

Application of ANN Modelling and GA Optimization for Improved Creep and Corrosion Properties of Spin-Arc Welded AA5083-H111 Alloy

V. Poonguzhali^a, T. Deepan Bharathi Kannan^b, M. Umar^a, and P. Sathiya^{a,*}

^aDepartment of Production Engineering, National Institute of Technology, Trichy, Tamilnadu, 620015 India

^bDepartment of Mechanical Engineering, SRM Institute of Science and Technology,
Kattankulathur, Tamilnadu, 603203 India

*e-mail: psathiya@nitt.edu

Received July 29, 2019; revised November 22, 2019; accepted November 26, 2019

Abstract—In this work, an attempt is made to identify the optimized parameter combination for improved creep and corrosion properties of AA5083-H111 alloy weldments processed by Spin-Arc gas metal arc welding (SA-GMAW) process. For this, the Artificial Neural Network (ANN) coupled with Genetic Algorithm (GA) was used as a statistical tool. Experiments were conducted by considering the input parameters namely welding current, filler spinning speed and filler spin diameter. The weld quality was assessed by measuring micro-hardness, corrosion resistance and steady-state creep rate. Initially, ANN was used to establish the relationship between input and output process variables. Different learning algorithms such as quick propagation (QP), back batch propagation (BBP) and incremental batch propagation (IBP) were used for predicting the output parameters. Prediction accuracy of the different learning algorithms was compared, and the best algorithm was used for the GA optimization technique. The optimum parameters were found to be 134 A of welding current, 1050 rpm of filler spinning speed and 1 mm of filler spin diameter. Among the input parameters, the filler spinning speed was identified as the most influential factor (40.11%) that effected the formation and distribution of second phase particles through which improved corrosion and creep properties were achieved.

Keywords: aluminum alloy, Spin-Arc GMAW, ANN, GA, corrosion, creep

DOI: 10.3103/S1067821220020091

1. INTRODUCTION

Lightweight materials are being continuously developed to meet the demands of aerospace, marine, automobile and biomedical industries. AA5083 alloy is one of the material which has many desirable properties such as high strength to weight ratio, lower density and very good corrosion resistance [1, 2]. AA5083 is a non-heat treatable alloy whose strength mainly depends on the amount of strain hardening. Magnesium is one of the main alloying elements in AA5083 [3]. AA5083 alloys are mainly used in the manufacturing of structural components in aerospace and marine industries [4]. Welding plays an important role in manufacturing of complicated structures of aerospace and marine components. Welding of AA5083 alloys is a little difficult owing to their physical properties such as higher thermal conductivity and high thermal expansion coefficient. It is known that exposure of AA5083 to a temperature of 200°C would result in the formation of Ab_3Mg_2 (β -phase) at the interdendritic regions. Formation of these β -phase particles significantly affected the corrosion behavior of high Mg alloys [5]. To date, works related to welding of AA5083

have been done using laser beam welding (LBW) and conventional metal inert gas (MIG) welding processes and tungsten inert gas (TIG) welding processes. Joining aluminum alloys using the LBW process encounters many practical challenges such as reflectivity of the laser and zero gap tolerance. The economical aspect of laser welding is also very high when compared with other conventional arc welding processes. Many researchers successfully explored the joining of AA5083 alloys using TIG and MIG welding processes. Umar et al. [6] compared the influence of filler wire diameter in pulsed TIG welding of AA5083 alloys and found that better strength and corrosion properties were obtained when the diameter of the filler wire was 2.4 mm. The authors found that the filler wire of bigger diameter produced a weld with equiaxed grains owing to the higher welding speed and lesser heat input. Yao Liu et al. [7] compared TIG and MIG welding in joining of AA5083 plates and found that TIG welding is suitable for AA5083 plates. MIG welding resulted in the formation of porosity, which in turn reduced weld strength. The major problem associated with narrow gap welding through conventional TIG

Table 1. The nominal composition of the base and filler metal (wt %)

Elements	Cu	Si	Fe	Mg	Mn	Cr	Ni	Ti	Zn	Al
AA5083-H111	0.02	0.12	0.4	4.57	0.94	0.06	0.01	0.027	0.02	Bal.
ER5356	–	–	–	5	0.12	0.12	–	0.12	–	Bal.

and MIG welding process is the molten pool sagging due to gravity, which in turn leads to defect formations. This problem could be overcome by the SA-GMAW process, where the filler wire is made to rotate between the plates to be welded. This phenomenon not only decreases the heat input supplied to the weld but also helps in counteracting the gravity of the upper side of the molten metal [8]. C.L. Yang [9] successfully joined low carbon plates of thickness 30 mm using SA-GMAW process. The authors concluded that the spin radius has a huge influence on the weld properties. The authors obtained weld with better properties when the spin radius was in the range of 2–3.6 mm.

The weld quality mainly depends on the process parameters and hence, importance should be given to the selection of correct parameter combinations. The selection of process parameters by trial and error method is timewasting and also not economical. The correct process parameters can be selected with the aid of modeling and optimization techniques, which would indeed result in higher weld quality and increased productivity. In recent times, the usage of ANN coupled with GA has gained much importance among the research community for identifying the optimized parameter combination. ANN works on the principle similar to biological neurons. ANN can guess the responses even with fewer data [10]. The accuracy of the prediction is very good when compared with the other modeling techniques. Muthukrishnan et al. [11] compared the prediction capability of regression ANN model with other ANN models in friction stir welding of AA6063 and A319. The authors concluded that the regression models are comparatively better than other ANN models in prediction accuracies. GA is a multiobjective optimization technique which works on principle based on natural genetics and natural selection. GA is very simple and easy to use. Choudhary et al. [12] compared the optimization techniques such as the genetic algorithm, Jaya algorithm, and the desirability approach in submerged arc welding of AISI 1023 steel and found that Jaya algorithm produced better optimization results compared to genetic algorithm and desirability approach. Deepan Bharathi Kannan et al. [13] utilized ANN along with a genetic algorithm for predicting the optimized parameter combinations in laser welding of NiTiInol shape memory alloys. The results obtained through GA were in good agreement with the confirmation results. The usage of ANN and GA is not only limited to welding processes but it has been explored in all sorts of the manufacturing process. Ali Solati et al. [14] used ANN-GA techniques for predicting the heat

affected zone width and bearing strength in the laser drilling of a fiber-reinforced polymer. The authors found that the ANN accuracy was better when the number of neurons in the hidden layer was 5 and 9.

From the literature, it is understood that no visible works have been done related to the welding of AA5083 alloy using SA-GMAW process and its corrosion and creep characteristics. Hence, an attempt is made in this work to join AA5083-H111 alloy sheets using SA-GMAW process and to study the corrosion, as well as creep properties of processed weldments. It is also understood from the literature that ANN and GA could be used for any manufacturing process for predicting the optimized parameter combinations. Hence in this work, ANN and GA techniques were used for predicting the optimized parameters that would result in better weld quality concerning microhardness, corrosion resistance and steady-state creep rate.

2. EXPERIMENTAL PROCEDURES

AA5083 plate of thickness 3 and 1.2 mm diameter ER5356 grade filler wire was used as a base and filler material, respectively. The base and filler material chemical composition are mentioned in Table 1. The Fronius Trans Synergic 4000 C model welding machine was used as a power source and it was coupled with a novel SpinArc GMAW torch (see Fig. 1) developed by Weld Revolution LLC, USA to produce the weld beads.

The experiments were conducted based on L9 Taguchi array taking welding current, filler diameter and filler spinning speed as input parameters. The ranges of the input welding parameters are presented in Table 2. The other welding parameters such as shielding gas flow rate, wire feed rate, travel speed, stick out distance, polarity, arc gap and filler diameter were maintained at a constant value and the corresponding values are presented in Table 3.

The L9 Taguchi array along with the input and output parameters are shown in Table 4.

The quality of the weld was assessed based on microhardness, corrosion resistance and steady-state creep rate. Vickers microhardness tester was used for calculating the microhardness value. Microhardness was measured based on the standard ASTM E8 by applying a load of 500 gf for a dwell period of 10 seconds. Microhardness was measured by taking the average of microhardness values at five 5 different points along the weld center. The corrosion resistance of the weld sample was measured using an electrochemical

Table 2. Input parameters and their levels

Factors/Levels	Level I (1)	Level II (0)	Level III (-1)
Welding current, A	120	130	140
Filler spinning speed, rpm	1050	1250	1450
Filler spin diameter, mm	1	2	3

Table 3. Constant welding parameters

Welding parameters	Value
Shielding gas flow rate, lpm	15
Wire feed rate, m/min	8.3
Travel speed, mm/sec	10
Stick-out distance, mm	22–24
Polarity	Electrode positive
Arc gap, mm	2
Filler diameter, mm	1.2

system in which the test sample was used as a working electrode, a standard calomel electrode was used as a reference electrode and a graphite rod was used as a counter electrode. All the electrodes were immersed in 3.5% NaCl solution for conducting the corrosion test. The electrode potential was varied from -1 to $+1$ V at a scan rate of 1 mV/s. Data acquisition was done by IVIUM soft electrochemistry software and the Tafel

analysis was used to determine the corrosion data in terms of passive region width (ΔE_{pit}):

$$\Delta E_{\text{pit}} = E_{\text{pit}} - E_{\text{corr}} \text{ (mV)}. \quad (1)$$

Where E_{pit} is the pitting potential; E_{corr} is the corrosion potential.

The steady-state creep rate was measured by using the impression creep testing machine. The analysis was performed by applying a constant load of 173 MPa for 3600 s at a temperature of 473 K [2, 4]. Metallurgical aspects of the weld obtained in the optimized parameters were analyzed using the microstructures obtained through electron backscatter diffraction (EBSD) analysis and high-resolution transmission electron microscope (HR-TEM). For metallurgical analysis, the samples were cut using wire EDM and the cut samples were mounted using cold mounting powder and liquid. Emery paper of different grades, viz. 200, 400, 600, 800, 1000, and 1200 were used for polishing the samples. Emery paper polishing was followed by velvet cloth polishing with the help of alumina powder. Samples were etched in Poulton's

**Fig. 1.** Image of SpinArc GMAW torch used for this work.

Table 4. L9 Taguchi array

Experiment no.	Welding current, A	Filler spinning speed, rpm	Filler spin diameter, mm	Microhardness, HV	Width of passive region, mV	Steady-state creep rate, $10^{-7}, s^{-1}$
1	1	1	1	74.8	361	3.81
2	1	0	0	72.3	352	4.11
3	1	-1	-1	70.33	304	4.15
4	0	1	0	77.23	381	2.89
5	0	0	-1	72.13	321	4.24
6	0	-1	1	68.9	309	3.65
7	-1	1	-1	73.1	313	3.6
8	-1	0	1	64.55	284	4.45
9	-1	-1	0	74.3	328	3.76

solution before performing the microstructural analysis [16].

2.1. Artificial Neural Network

ANN is a mathematical modeling tool that works similar to biological neurons. There are 3 different layers in neural network viz. input, hidden and output layer. The input layer neurons denote the independent variables which have control of the output variables associated with the manufacturing process. The input data received in the input layer are processed in the hidden layer. Depending on the problem complexity and accuracy, the hidden layers may be one or two or three, etc. The neurons in each hidden layer also vary and there are no established results stating that this number of hidden layers will result in better accuracy. The output layer collects the information from the hidden layer and transmits the information as per the requirement. The neurons in the output layer depend on the number of output variables considered in the manufacturing process. ANN modeling involves two steps, viz. training and testing. In general, 80 and 20% of the input data are used for training and testing the neural network respectively.

2.2. Genetic Algorithm

GA is one of the optimization techniques that works based on the principle of species evolution by natural selection. The steps involved in GA are population initialization, evaluation of objective function, finding fitness function and application of genetic operators like reproduction, mutation, and cross over until the stopping criteria.

The parameters associated with GA were selected based on the literature [15]. The GA parameters used in this work are as follows: the population size considered for the GA analysis was 100, mutation and crossover rate selected were 0.01 and 0.9 respectively. In

addition to that, Single-point crossover was considered along with the roulette method selection type.

3. RESULTS AND DISCUSSIONS

3.1. ANN Modelling

In this work, modeling was done using different learning algorithms viz., QP, IBP and BBP. The hidden layer was varied from one to two and at the same time, the neurons in each hidden layer were varied from 4 to 20.

The prediction accuracy of the learning algorithms was calculated on the basis of the root mean square error (RMSE) value. RMSE value was calculated using Eq. (2)

$$RMSE = \sqrt{\frac{1}{n} \sum_{i=1}^n (A - B)^2}, \quad (2)$$

where A denotes the experimental value, B denotes the predicted value and n denotes the number of testing data.

Tanh function was used for both the hidden layer and the output layer. The tanh function is presented in Eq. (3).

$$F(x) = \frac{1 - \exp(-ax)}{1 + \exp(-ax)}, \quad (3)$$

RMSE value of different learning algorithms was calculated using Eq. (2) are shown in Table 5.

From the above table, it can be understood that the BBP with two hidden layers and 10 neurons in each hidden layer produced the least RMSE value signifying that, it is the best learning algorithm.

The data obtained through the BBP training process is presented in Tables 6 and 7. Likewise, the data obtained through the testing process is presented in Table 8.

The ANN structure obtained for the best learning algorithm is shown in Fig. 2.

Table 5. RMSE value of learning algorithms

No. of neurons	QP		IBP		BBP	
	hidden layer-1	hidden layer-2	hidden layer-1	hidden layer-2	hidden layer-1	hidden layer-2
4	0.2650	0.4344	1.2009	0.3043	0.6062	0.3749
5	3.3070	0.0001	0.1532	0.2588	0.2727	0.9264
6	0.2223	0.0011	0.8421	0.0858	0.2303	0.1513
7	0.2072	0.5582	0.3719	0.0099	0.1728	0.0226
8	0.4172	0.0018	0.6740	0.0069	0.0626	0.1738
9	0.0810	0.0005	0.1702	0.0705	0.3810	0.0643
10	0.2436	0.0179	0.2582	0.0473	0.2422	0.0001
15	0.0177	0.0027	0.3822	0.0243	3.3436	0.0304
20	2.9178	0.0007	0.0955	0.0084	0.4267	0.2048

Table 6. Training data for microhardness and width of passive region

Observed microhardness, HV	Calculated microhardness, HV	Difference, 10^{-5} , HV	Observed width of passive region, mV	Calculated width of passive region, mV	Difference, 10^{-4} , mV
74.8	74.8	14.9	361	361	2.5
72.3	72.3	3.93	352	352	1.07
70.33	70.33	1.63	304	304	1.8
77.23	77.23	0.68	381	381	0.32
72.13	72.13	1.56	298	298	0.22
68.9	68.9	1.66	309	309	1.3
73.1	73.1	18.3	313	313	1.45

Table 7. Training data for steady-state creep rate

Observed steady-state creep rate, 10^{-7} , s^{-1}	Calculated steady-state creep rate, 10^{-7} , s^{-1}	Difference, s^{-1}
3.80	3.80	1.11×10^{-12}
4.11	4.11	8.99×10^{-14}
4.15	4.15	5.60×10^{-13}
2.89	2.89	1.96×10^{-13}
4.24	4.24	1.77×10^{-13}
3.65	3.65	4.57×10^{-13}
3.60	3.60	1.81×10^{-13}

Table 8. Testing data

Experiment no.	Welding current, A	Filler spinning speed, rpm	Filler spin diameter, mm	Microhardness, HV	Width of passive, region, mV	Steady-state creep rate, 10^{-7} , s^{-1}
8	140	1250	1	69.82	329	3.17
9	140	1450	2	69.19	302	3.82

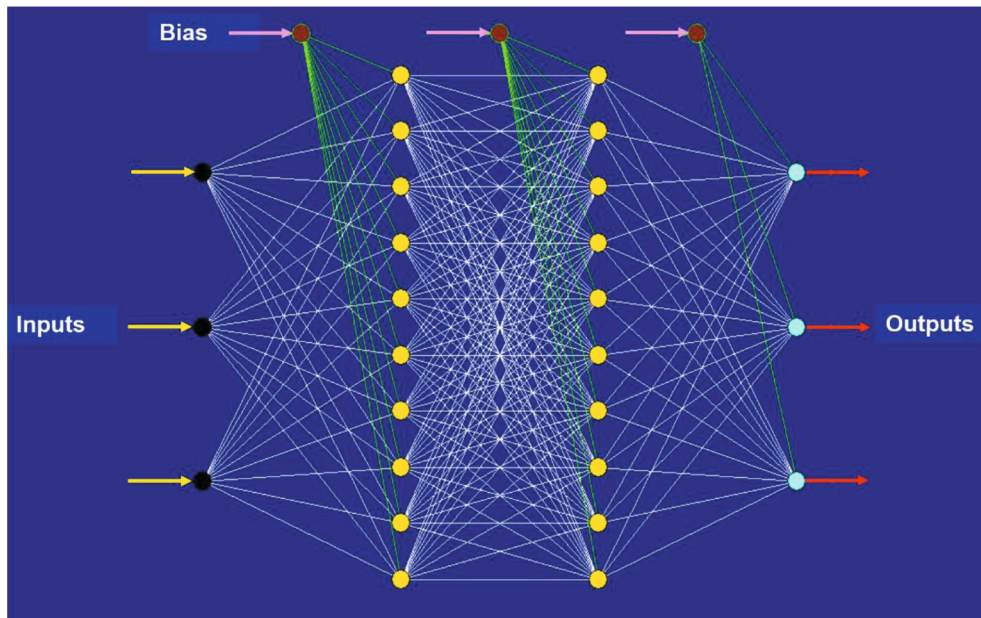


Fig. 2. ANN structure for the best learning algorithm.

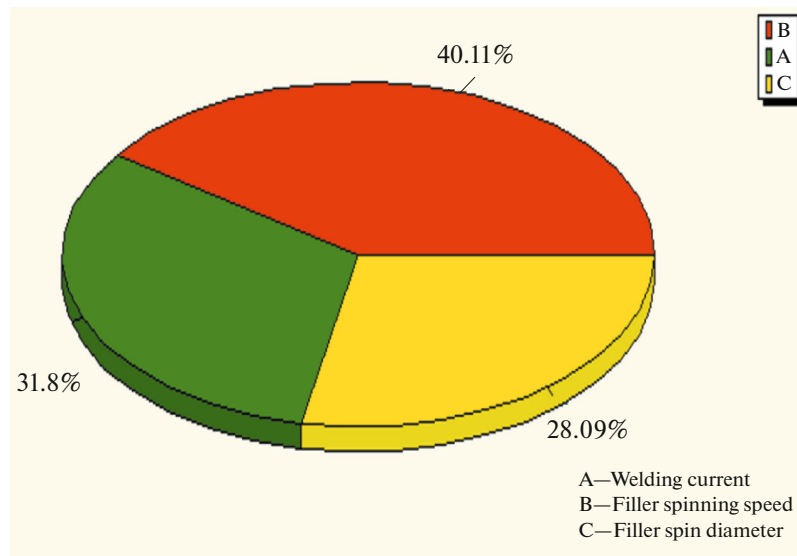


Fig. 3. Percentage of Importance on the overall objective function.

The most influencing parameter based on the ANN was identified as filler spinning speed followed by welding current and filler spin diameter. The influence of input parameters on the multi-objective function is presented in Fig. 3. A, B, and C in Fig. 3 denote welding current, filler spinning speed and filler spin diameter respectively.

BBP learning algorithm with 2 hidden layers and 10 neurons was interfaced with GA to find the optimized parameters.

The step involved in ANN-GA is presented in Fig. 4.

3.2. GA Optimization

The lower and upper bound value for welding current, filler spinning speed, filler diameter were 120 and 140 A, 1050 and 1450 rpm, 1 and 3 mm respectively. The Optimized parameter combination identified through GA is shown in Table 9.

From Table 9, it can be understood that the confirmation test results were in agreement with the values obtained through GA. The maximum deviation from the predicted value was around 3.9% only.

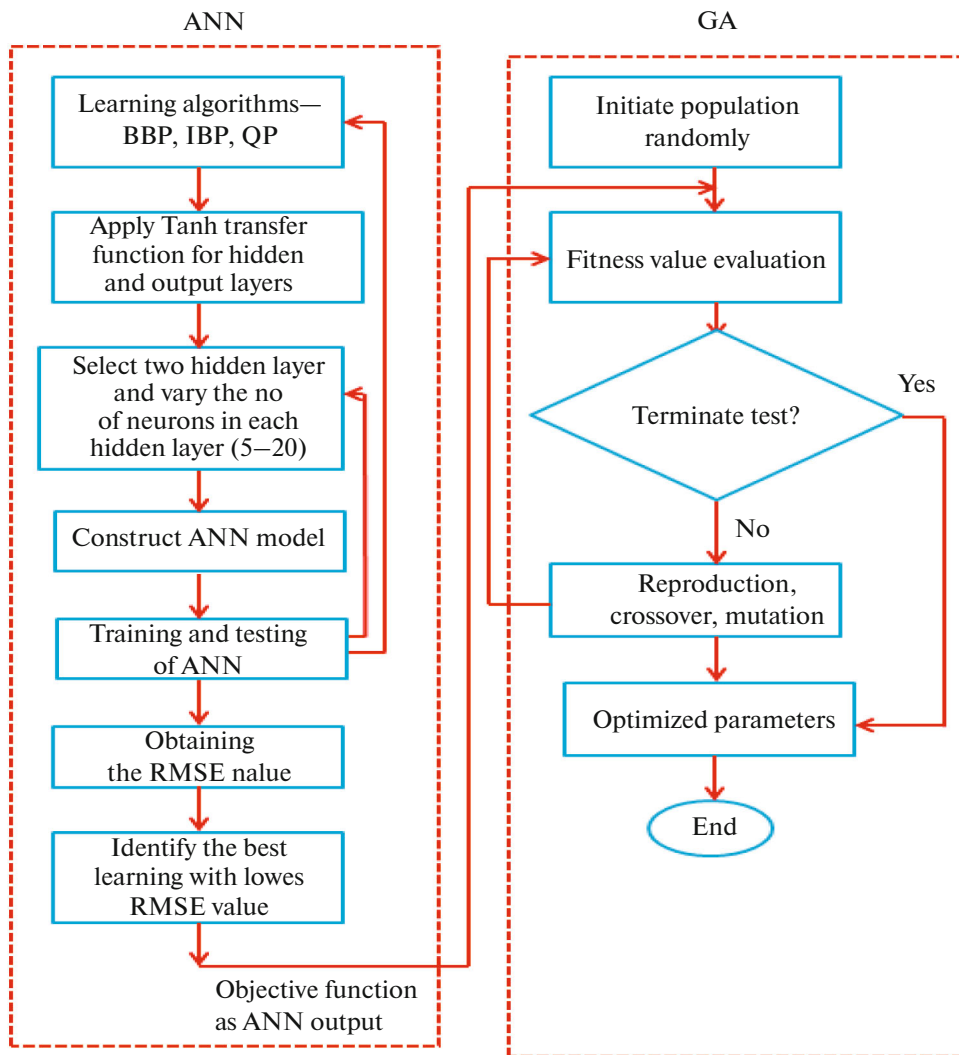


Fig. 4. ANN–GA working methodology [13].

3.3. Confirmation Test

A confirmation test was conducted based on the optimized parameters. The microstructure, microhardness, corrosion and creep properties of the weld were analyzed.

3.3.1. Microstructure of the optimized weld. Figures 5a–5d show the microstructure of the weldment

processed at an optimized condition, i.e., welding current of 134 A, the filler rotation speed of 1050 rpm and filler spinning diameter of 1 mm. It is apparent from Figs. 4b–4d that the transformation of grains shape from cellular to equiaxed dendrites ensued at the middle of the weld (FZ) from the base metal. The typical directionally solidified microstructure was attained in

Table 9. Optimized parameters and confirmation test

Experiment	Welding current, A	Filler spinning speed, rpm	Filler spin diameter, mm	Microhardness, HV	Width of passive region, mV	Steady-state creep rate, $10^{-7}, s^{-1}$
GA optimal solution	134.77	1050.26	1.27	77.07	389	2.85
Feasible solution	134	1050	1	74	385	2.75
Error percentage				3.9%	1.32%	3.50%

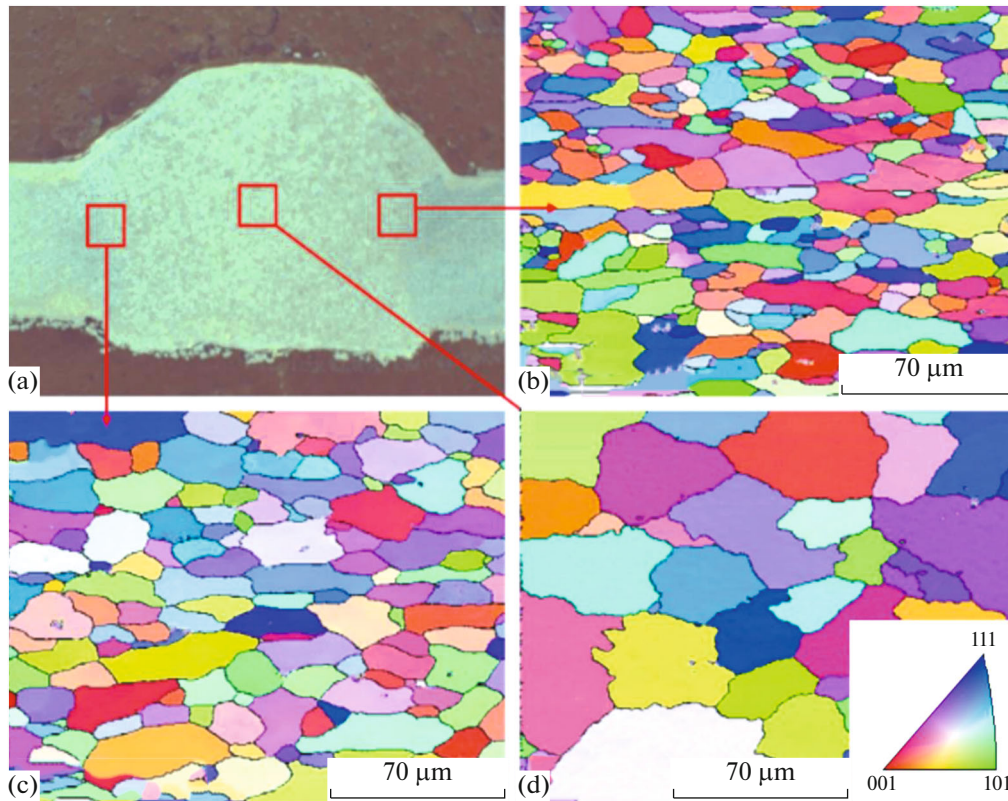


Fig. 5. Macro and microstructure of optimized weld: (a) Cross-sectional view of the weldment. (b) EBSD microstructure of the right sidewall. (c) Left sidewall. (d) FZ.

the middle of the weld bead due to the difference in solidification velocity and the formation of equiaxed dendrites at the weld FZ was evident owing to the increased cooling rate associated with GMAW process. The average grain size at the FZ (Fig. 5d) was observed to be $46.73 \mu\text{m}$, which is higher than that of base metal ($21.52 \mu\text{m}$). Furthermore, the nano-scale microstructural features of the optimized weld were observed under HR-TEM and the results are presented in Fig. 6. From Fig. 6, it is observed that the FZ of processed weld consists of Mg, Fe and Mn-rich second phase particles at the grain boundaries and grain interiors.

Figure 6a shows the grain boundary precipitation of β -phase (Al_3Mg_2) particle and the P-phase particles are often seen in high Mg ($>4.5\%$) alloys and it can be continuous or discontinuous along the boundaries [1–3]. Figure 6b illustrates the high density of dislocation bands, which could act as an obstacle during mechanical loading. Figure 6c confirms the existence of rod-like, plate-like and spherical Fe or Mn-rich intermetallic particles at the FZ. The plate-like and spherical particles appeared dark in the dark-field image (Fig. 6d), suggesting it contains higher atomic elements like Fe and Mn. The rod-like particle appeared to be bright in the dark-field image and the corresponding EDS spectrum (Fig. 6e) confirms that

it is an Al_6Mn particle. The development of such Mn-rich intermetallic constituents at the grain boundaries as well as grain interiors, could improve the corrosion properties and strength of the weld [4–6].

3.3.2. Corrosion resistance of the optimized weld. The corrosion characteristics of the FZ of the optimized weld were observed through the potentiodynamic polarization test and the corrosion curve is shown in Fig. 7. The width of passive region (ΔE_{pit}) was determined (385 mV) from the curve and it is evident that the optimized weld showed the highest width of passive region among the weldments. The presence of a higher number of cathodic Fe and Mn-rich particles (see Fig. 6c) resist continuous pitting attack and thereby result in noble corrosion resistance among the samples.

3.3.3. Creep resistance of the optimized weld. Creep resistance of the optimized weld was determined using the impression creep test on the FZ of weldment at a temperature of 473 K with punching stress of 130 MPa. The displacement of indenter (impression depth) was documented continuously as a function of time and using the data; a creep curve was drawn between the impression depth and time (see Fig. 8). From that, a steady-state creep rate, and the impression velocity of FZ of weldment were determined. It is apparent from Fig. 8 and Table 9 that the lowest creep rate

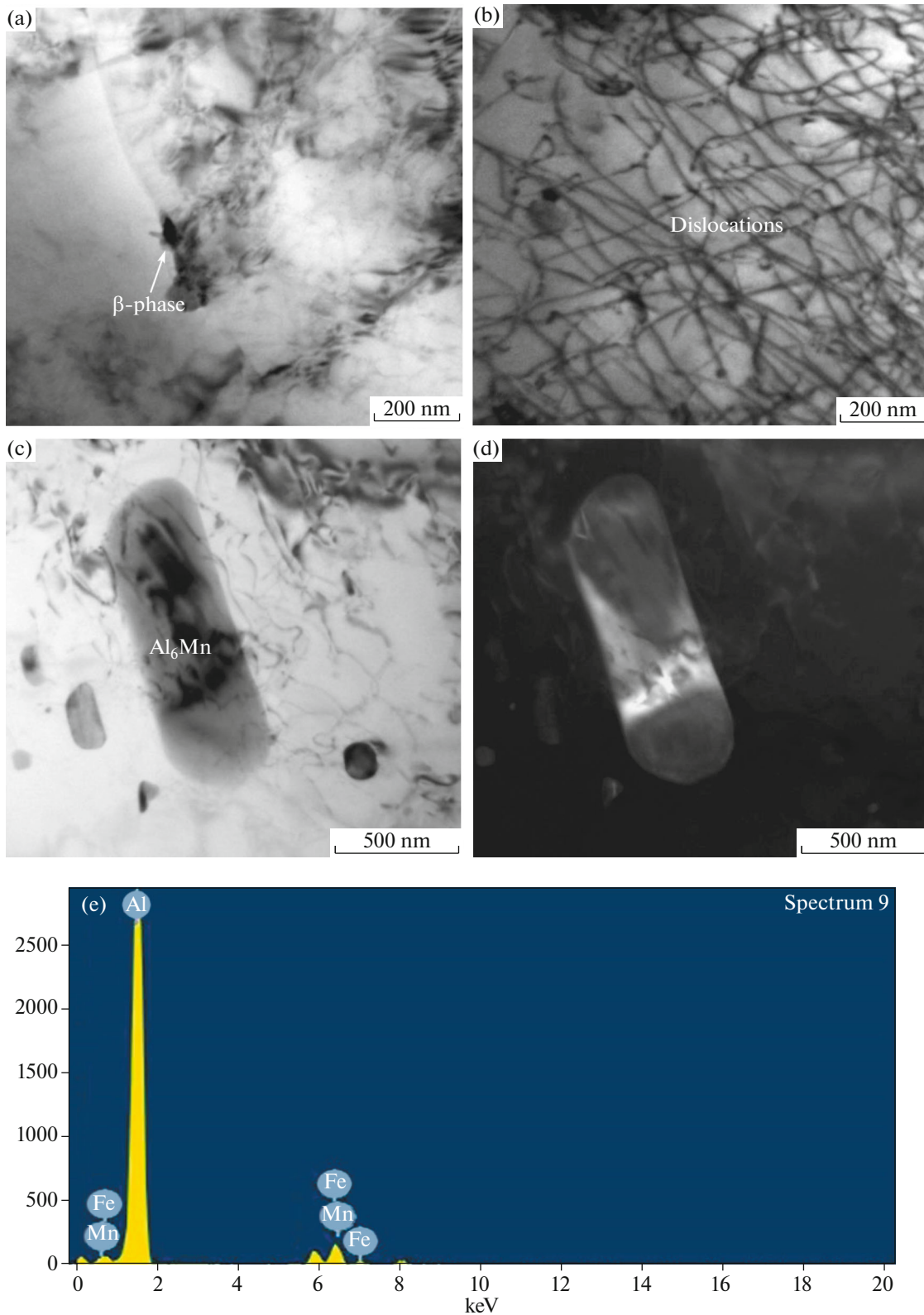


Fig. 6. HR-TEM shows the fine-scale microstructure of FZ: (a) Bright-field image shows β -phase precipitate at the grain boundary. (b) High-density dislocation bands exist at the grain interior. (c) Bright-field image of rod-like Mn-rich intermetallic particle. (d) Dark-field image of (c). (e) EDS spectrum taken on the rod-like particle shown (c).

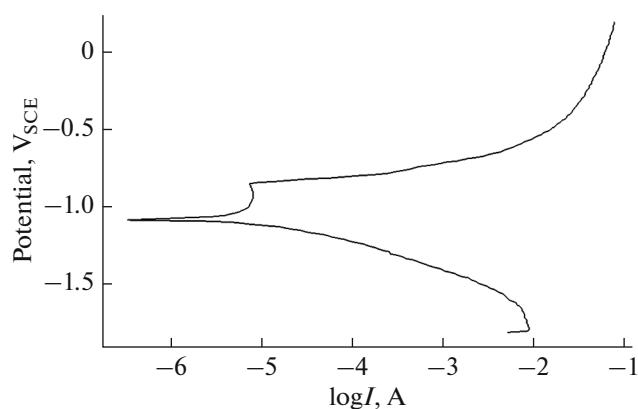


Fig. 7. Potentiodynamic polarization curve for the optimized weld.

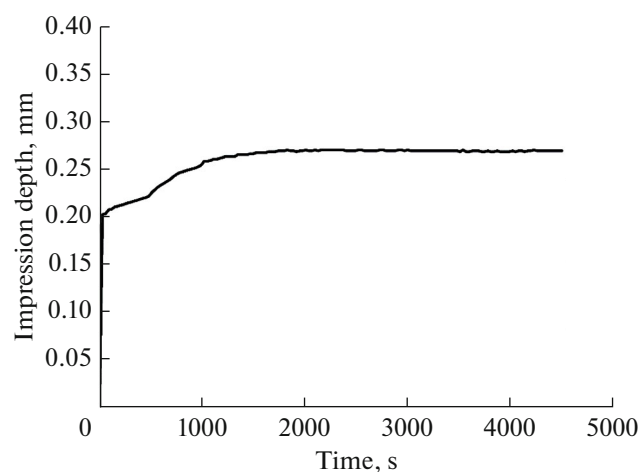


Fig. 8. Impression depth versus time plot for the optimized weld.

($2.75 \times 10^{-7} \text{ s}^{-1}$) was attained in the optimized weld sample. The increase in creep resistance could be attributed to the existence of finer Fe and Mn-rich intermetallic particles at grain interior as well as boundaries.

4. CONCLUSIONS

In this study, a Taguchi based L9 design was employed to design the parameters and joining of AA5083-H111 alloy was successfully carried out using Spin-Arc GMA welding process. The ANN coupled with GA algorithm techniques were applied to optimize the three process parameters of Spin-Arc GMAW process on the creep and corrosion properties of weldments. The following conclusions are drawn from the investigation:

- All three factors welding current, filler spinning speed and filler spin diameter are found to be the most influential parameters on the creep and corrosion

properties. Among the factors, the filler spinning speed had a significant influence (40.11%) on the weld properties.

- The optimal levels of various Spin-Arc GMAW process parameters for the highest creep and corrosion properties were 134 A of welding current, 1050 rpm of filler spinning speed and 1 mm of filler spin diameter.

- The confirmation test was carried out with optimum parameters and the percentage deviation between the experimental and predicted values was less than 4% for all the output responses. It shows that the developed model can be effectively used to predict the corrosion and creep properties of Spin-Arc GMA welded joints.

- The improvement in creep strength, corrosion resistance and hardness of the optimized weld were attributed to the high density of dislocations and nano-scaled cathodic particles formed at the grain boundaries as well as grain interiors.

REFERENCES

1. Gaosong Yi, Binhan Sun, Poplawsky, J.D., Yakun Zhu, and Free, M.L., Investigation of pre-existing particles in Al 5083 alloys, *J. Alloys Compd.*, 2018, vol. 740, pp. 461–469.
2. Mustafa Umar and Paulraj Sathiya, Influence of melting current pulse duration on microstructural features and mechanical properties of AA5083 alloy weldments, *Mater. Sci. Eng., A*, 2019, vol. 746, pp. 167–178.
3. Goswami, R., Spanos, G., Pao, P.S., and Holtz, R.L., Precipitation behavior of the β phase in Al-5083, *Mater. Sci. Eng., A*, 2010, vol. 527, pp. 1089–1095.
4. Mustafa Umar and Paulraj Sathiya, Effect of pulse duration on corrosion and impression creep properties of AA5083-H111 Al-Mg alloy weldments processed by P-GTAW, *Adv. Eng. Mater.*, 2018, vol. 20, no. 6. <https://doi.org/10.1002/adem.201701147>
5. Goswami, R. and Holtz, R.L., Transmission electron microscopic investigations of grain boundary beta phase precipitation in Al 5083 aged at 373 K (100°C), *Metall. Mater. Trans. A*, 2013, vol. 44, pp. 1279–1289. <https://doi.org/10.1007/s11661-012-1166-9>
6. Umar Mustafa, Mukesh Chandra, and Sathiya Paulraj, Influence of filler wire diameter on mechanical and corrosion properties of AA5083-H111 Al-Mg alloy sheets welded using an AC square wave GTAW process, *Trans. Indian Inst. Met.*, 2018, vol. 71, no. 8, pp. 1975–1983.
7. Yao Liu, Wenjing Wang, Jijia Xie, Shouguang Sun, Liang Wang, Ye Qian, Yuan Meng, and Yujie Wei, Microstructure and mechanical properties of aluminum 5083 weldments by gas tungsten arc and gas metal arc welding, *Mater. Sci. Eng., A*, 2012, vol. 549, pp. 7–13.
8. Matsuda, F., *Narrow Gap Welding*, Osaka: Japan Welding Society/Kuroki Press, 1984.
9. Yang, C.L., Guo, N., Lin, S.B., Fan, C.L., and Zhang, Y.Q., Application of rotating arc system to horizontal narrow gap welding, *Sci. Technol. Weld. Joining*, 2009, vol. 14, no. 2, pp. 172–177. <https://doi.org/10.1179/136217108X388651>

10. Tarun Kumar Gupta and Khalid Raza, Optimization of ANN architecture: a review on nature-inspired techniques, in *Machine Learning in Bio-Signal Analysis and Diagnostic Imaging*, Academic Press, 2019, chap. 7, pp. 159–182.
<https://doi.org/10.1016/B978-0-12-816086-2.00007-2>
11. Krishnan, M.M., Maniraj, J., Deepak, R., and Anganan, K., Prediction of optimum welding parameters for FSW of aluminium alloys AA6063 and A319 using RSM and ANN, *Mater. Today: Proc.*, 2018, vol. 5, pp. 716–723.
12. Ankush Choudhary, Manoj Kumar, and Deepak Rajendra Unune, Experimental investigation and optimization of weld bead characteristics during submerged arc welding of AISI 1023 steel, *Def. Technol.*, 2019, vol. 15, pp. 72–82.
13. Deepan Bharathi Kannan, T., Ramesh, T., and Sathiya, P., Application of artificial neural network modelling for optimization of Yb: YAG laser welding of nitinol, *Trans. Indian Inst. Met.*, 2017, vol. 70, pp. 1763–1771.
14. Solati, A., Hamed, M., and Safarabadi, M., Combined GA-ANN approach for prediction of HAZ and bearing strength in laser drilling of GFRP composite, *Opt. Laser Technol.*, 2019, vol. 113, pp. 104–115.
15. Sathiya, P., Pannerselvam, K., and Abdul Jaleel, M.Y., Optimization of laser welding process parameters for super austenitic stainless steel using artificial neural networks and genetic algorithm, *Mater. Des.*, 2012, vol. 36, pp. 490–498.
16. Rastkerdar, E., Shamanian, M., and Saatchi, A., Taguchi optimization of pulsed current GTA welding parameters for improved corrosion resistance of 5083 aluminum welds, *J. Mater. Eng. Perform.*, 2013, vol. 22, pp. 1149–1160.